

Effect of Hydrogen Charging on the Stress Corrosion Behavior of 2205 Duplex Stainless Steel Under 3.5 wt.% NaCl Thin Electrolyte Layer

Tianliang Zhao, Zhiyong Liu, Shanshan Hu, Cuiwei Du, and Xiaogang Li

(Submitted December 5, 2016; in revised form April 3, 2017; published online May 8, 2017)

The effect of hydrogen charging on the stress corrosion cracking (SCC) behavior of 2205 duplex stainless steel (DSS) under 3.5 wt.% NaCl thin electrolyte layer was investigated on precharged samples through hydrogen determination, electrochemical measurement, and slow strain rate tensile test. Results show that hydrogen charging weakens the passive film without inducing any obvious trace of localized anodic dissolution. Therefore, hydrogen charging increases the SCC susceptibility of 2205 DSS mainly through mechanism of hydrogen embrittlement rather than mechanism of localized anodic dissolution. 2205 DSS shows a more susceptibility to hydrogen under the TEL when hydrogen charging current density (HCCD) is between 20 and 50 mA cm⁻². The increasing trend is remarkable when hydrogen charging current density increases from 20 to 50 mA cm⁻² and fades after 50 mA cm⁻².

Keywords 2205 duplex stainless steel, hydrogen charging, stress corrosion, thin electrolyte layer

1. Introduction

Steel structures last for decades in dry parts of inland, but fail within months in humid and salty coastal areas (Ref 1). Most of these failures are caused by corrosion under thin electrolyte layer (TEL) (Ref 2, 3). A strong corrosive TEL forms on metal surfaces near sea level due to high humidity, salinity, and long wetting time, especially in subtropical and tropical sea areas (Ref 4, 5). Thus, severe localized corrosions are often observed under TEL at marine atmosphere with high temperature and increasing salinity concentration caused by cyclic wet–dry process (Ref 3, 6–8).

Many studies (Ref 9–13) systematically revealed that hydrogen reductions extensively exist during corrosion under wet–dry cycles in marine atmosphere. For example, Huang et al. (Ref 10) found that hydrogen permeation current is produced during wet stages; this current increases with increased concentration of Cl⁻ and SO₄²⁺ under the TEL. Generally, hydrogen reduction during wet–dry cycles is as follows (Ref 11, 12): The wet–dry cycles concentrate ions inside the local blocking sites, such as pits under product layer and crevices in junctions. The hydrolyzation of Fe²⁺ ions inside these localized blocking sites acidifies the local environment. Abundant chlorides in marine atmosphere also promote acidification. The resulting H⁺ ions

weaken the passive film with chloridion joint and promote anodic dissolution. The Fe²⁺ ions newly generated by anodic dissolution are hydrolyzed, thereby producing many H⁺ ions. The repeating process continuously acidifies the medium in those local blocking sites. Huang et al. (Ref 9) verified by direct measurement that the pH beneath the water film and rust layer can be approximately 4.5. Consequently, hydrogen evolution reactions are promoted with increasing concentration of H⁺ ion. Therefore, hydrogen embrittlement (HE) or hydrogen-induced stress corrosion in steels might still occur in marine atmosphere (Ref 14–16). Ma et al. (Ref 17) studied the stress corrosion behaviors of E690 steel under marine atmosphere. They found that cathodic reactions are controlled by both oxygen diffusion and hydrogen reduction. Moreover, the resulting FeSO₄ promotes reproduction of hydrogen ions, which induce the stress corrosion cracking (SCC) of E690 under marine TEL. Li et al. (Ref 18) evaluated the susceptibilities of high-strength steels to delay fracture; they found that the fracture stresses of AISI 4135 steels decrease with increased diffusible hydrogen content, which increases with wet–dry cycles. Tsuru et al. (Ref 19) indicated that the hydrogen evolution mechanism on passive films is different from that on a bare iron surface, which enhances hydrogen permeation. Zhang et al. (Ref 20) investigated the HE of galvanized steel in simulated marine atmosphere. Their results showed that galvanized steel exhibits high HE susceptibility in marine atmosphere. This susceptibility is also affected by the relative humidity and the zinc coating coverage. Therefore, the hydrogen behavior and its effects on stress corrosion of steels at marine atmosphere or under TEL are complicated, and they need further investigations. Moreover, reports focusing on the effect of hydrogen on stress corrosion of stainless steel under marine atmosphere or TEL are few given.

Due to its relatively high strength and good resistance to pitting and SCC, duplex stainless steel (DSS) is extensively applied in some severe environments (Ref 21–26). However, DSS is attacked by SCC in marine atmosphere (Ref 4, 27–30). Glowacka et al. (Ref 31) found that α phase in DSS gradually decays, in addition, the stacking faults in γ phase significantly

Zhao Tianliang, Liu Zhiyong, Hu Shanshan, and Du Cuiwei, Corrosion and Protection Center, University of Science and Technology Beijing, Beijing 100083, China; **Li Xiaogang**, Key Laboratory of Chinese Ministry of Education for Corrosion and Prevention, University of Science and Technology Beijing, Beijing 100083, China; and Ningbo Institute of Material Technology & Engineering, Chinese Academy of Sciences, Ningbo 315201, China. Contact e-mail: Liuzhiyong7804@126.com.

increase with prolonged hydrogen charging time; this increase is probably related to strong grain refinement. However, the relation between stress corrosion and microstructure under hydrogen charging is not considered in their study. Zakroczyński et al. (Ref 32) revealed that the reduced ductility of steel is closely associated with the hydrogen concentration cathodically charged hydrogen. In their other research (Ref 33, 34), they found that hydrogen behaves differently in α and β phases: Diffusible hydrogen in ferrite matrix and reversibly trapped hydrogen in austenite phase induce different concentrations in different phases. Luu et al. (Ref 35) also detected large hydrogen distribution and high permeation and diffusion rates in ferritic phase. Kheradmand et al. (Ref 36) also found that the hydrogen effects on different phases are strongly associated with the existing residual stress, and these effects differ in each phase. Silverstein et al. (Ref 37, 38) applied two advanced techniques, namely thermal desorption spectrometry and secondary ion mass spectrometer, on examining the local hydrogen concentration, trapping, and distribution in 2205 DSS; their study provided further understanding regarding the HE mechanism of DSS. Although considerable efforts have been devoted to determine how hydrogen affects the mechanical properties of DSS, most of the existing reports have ignored the role of environment, such as the scale effect of TEL.

In the present work, a typical DSS, namely 2205 DSS, was used as the experimental material. The electrochemical and stress corrosion behaviors of 2205 DSS charged with different densities of cathodic current were investigated under 3.5 wt.% NaCl TEL by electrochemical measurements, slow strain rate tensile (SSRT) tests, and fracture surface characterizations. The effect of hydrogen on the SCC behavior of 2205 DSS under TEL was discussed. Conclusions were drawn on the basis of the results.

2. Materials and Experiments

2.1 Materials and Sample Preparation

The 2205 DSS was used as-received. The chemical composition is listed in Table 1. The metallographic microstructure is shown in Fig. 1. Carbon and sulfur contents were measured by infrared absorption method. Other contents were measured by inductively coupled plasma atomic emission spectrometry. The metallographic microstructure was obtained by etching the polished matrix using aqua regia; the volume ratio of HNO₃ (16 mol/L) to HCl (12 mol/L) is 1:3. Austenite (white areas) and ferrite (gray areas) phases are distributed alternatively and uniformly with approximately equal volume shared. The mechanical properties of the studied 2205 DSS were evaluated according to the standard GB/T 228-09. The test was performed on a MTS Landmark 370 material test system. Size of the specimens is shown in Fig. 2. The proof stress ($\sigma_{p0.2}$), tensile strength (σ_b), elongation (δ), and reduc-

tion-in-area (ϕ) of the 2205 DSS are 583 MPa, 777 MPa, 19.6%, and 58.6%, respectively.

Specimens for hydrogen charging and determination and electrochemical measurements were machined plates with dimensions of $\phi 5.64$ mm \times 3 mm. The specimens were welded to a copper wire for electric connection and mounted in epoxy resin with an exposed area of 10 mm². The exposed surface was progressively ground with emery to 1500 grit, cleaned with deionized water and alcohol, and dried with a blower.

Specimens for SSRT tests were machined according to the standard GB/T15970.7-2000. The specimen size is shown in Fig. 2. The working section was ground with emery paper to 1500 grit, then degreased with alcohol, and rinsed with deionized water. The specimens were covered with silica gel, and the working section was left exposed.

2.2 Hydrogen Charging and Determination

Hydrogen was introduced in advance in the matrix by electrochemical method. The charging solution was aqueous with NaOH (0.25 M) and thiourea (0.25 g/L). Pure nitrogen was piped in the solution for 2 h to deaerate before charging. A typical three-electrode system was applied for hydrogen charging; this system included a 2205 DSS specimen as the working electrode (WE), a saturated calomel electrode (SCE) as the reference electrode (RE), and a platinum plate as the counter electrode (CE). Constant cathodic currents of 10, 20, 50, and 100 mA cm⁻² were applied on specimens. In this study, the hydrogen charging current density (HCCD) magnitude may be considerably higher than the magnitude in actual service. The hydrogen content of substrate in actual service resulted from years of accumulation. HCCD in laboratory should be tens or hundreds of times that of hydrogen reduction current density in free and actual corrosion so that it can simulate the actual hydrogen content of the substrate after years

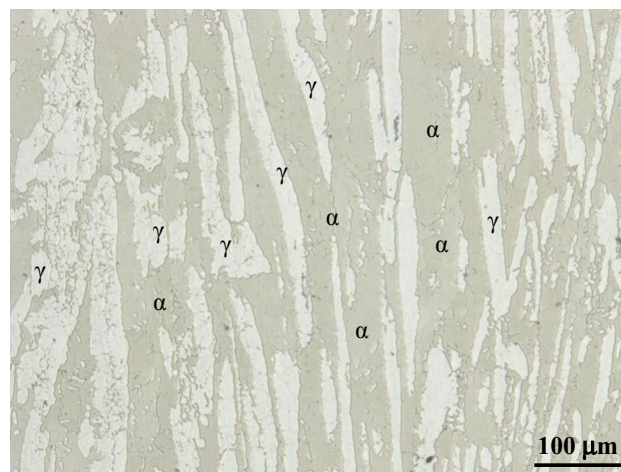


Fig. 1 Optical microstructure of 2205 DSS

Table 1 Chemical composition of the 2205 duplex stainless steel (wt.%)

C	Si	Mn	P	S	Cr	Ni	Mo	N	Fe
0.029	0.59	1.20	0.029	0.004	22.57	4.63	2.62	0.13	Balance

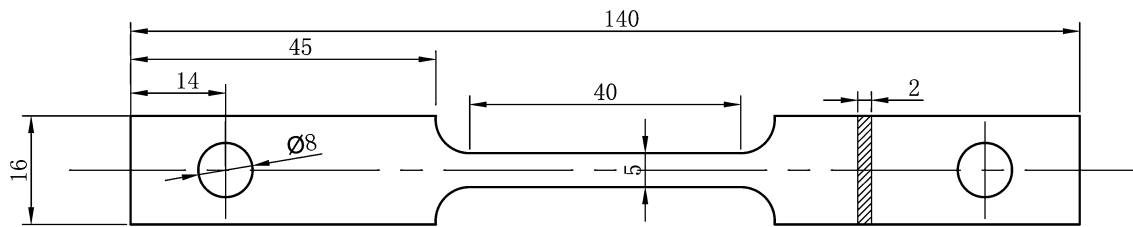


Fig. 2 Size of specimens used for mechanical testing

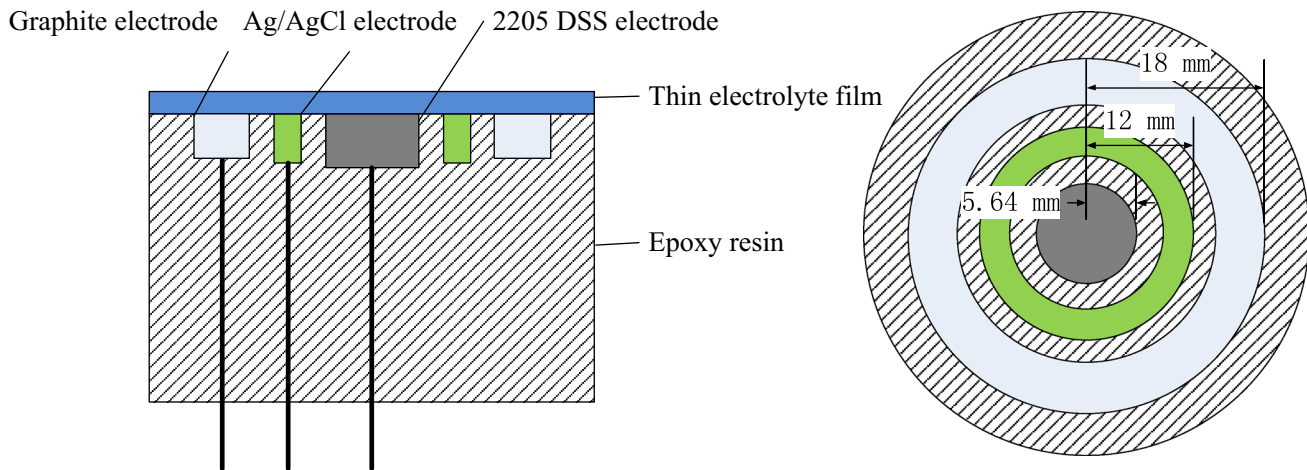


Fig. 3 Sketch of electrode capsule for electrochemical measurement under thin electrolyte layer (TEL)

of service. This HCCD magnitude was also adopted in many previous studies (Ref 39, 40). Hydrogen charging continued for 24 h for each experiment. According to the method above, specimens for hydrogen determination, electrochemical measurements, and SSRT tests were precharged cathodically.

The three-electrode system was also used for hydrogen determination. Specimens were rinsed with NaOH (0.2 M) solution immediately after charging and placed in NaOH (0.2 M) solution for hydrogen determination. Pure nitrogen was piped in the solution for 2 h before the determination and continuously piped during determination. Specimens were positively polarized to 168 mV (versus SCE). Subsequently, the polarization current was recorded as a function of time. A specimen without hydrogen charging was also prepared using the same process as the blank control. The hydrogen oxidation current was varied with time by subtracting the polarization current of the blank specimen from that of the charged specimen. Hence, the hydrogen content introduced in the charged specimen was quantified by integrating oxidation current on time.

2.3 Electrochemical Measurement

The electrochemical measurements conducted on the precharged specimens under TEL included potentiodynamic polarization and electrochemical impedance spectroscopy (EIS) measurements. The setup for electrochemical measurements under TEL was in accordance with that in the literature (Ref 3). The WE, RE, and CE were encapsulated together with epoxy resin (Fig. 3) and gradually ground with emery paper to 1500 grits. Prior to measurement, specimen was

hydrogen-charged according to the method mentioned in section 2.2. Afterward, the capsule was placed on a horizontal platform within 3.5 wt.% NaCl atmosphere for 2 h to form a steady TEL on its surface. During the measurement, temperature was kept at 30 ± 2 °C. The TEL thickness was measured by a device consisting of ohmmeter, screw micrometer, and bronze needle and kept at around 100 μm by controlling the salt mist flow rate. The thickness (100 μm) utilized in this study was within the range of that adopted by most previous studies (Ref 41, 42). A Princeton VMPS electrochemical workstation was used to acquire data. All potential data were obtained versus SCE. For potentiodynamic polarization measurements, the potential scanning rate was 0.5 mV/s, and the potential polarization ranged from -750 to 2000 mV versus open circuit potential. For EIS measurements, the test frequency ranged from 10 kHz to 0.1 Hz, and the AC amplitude was 10 mV. A software ZsimpWin V3.20 was used to fit the EIS data.

2.4 SSRT

SSRT tests were carried out on the charged specimens with a material test system (Letry Co., Ltd., Model: WDML-3). The setup used for SSRT test under TEL is depicted in Fig. 4. Mist nebulized from 3.5 wt.% NaCl solution was continuously injected in the box to form a TEL on the working section. To keep the TEL thickness at approximately 100 μm (same as that of electrochemical measurement), the flow rate was consistent with that of the electrochemical measurement. The temperature was also kept at 30 ± 2 °C. The tensile test began after 2 h of mist injection. The tensile rate was 0.0012 mm/min.

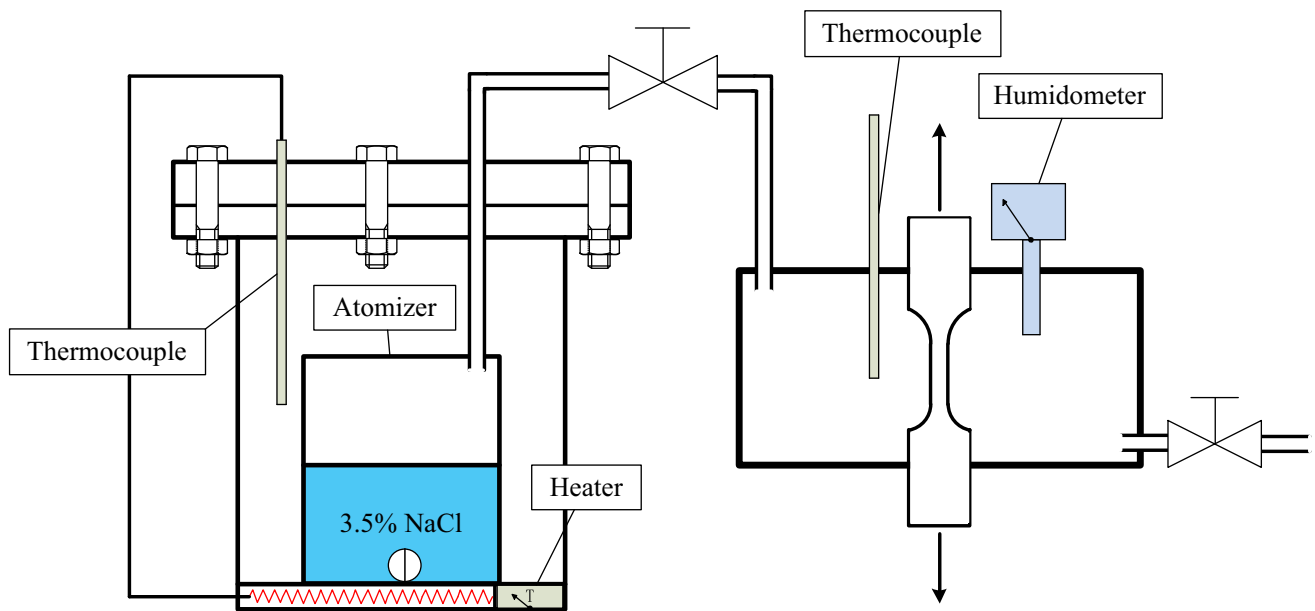


Fig. 4 Setup used for slow strain rate tensile (SSRT) test under TEL environment

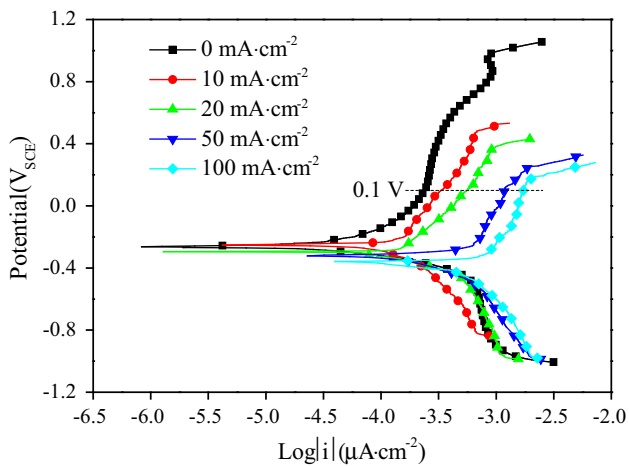


Fig. 5 Effect of hydrogen charging current density (HCCD) on the potentiodynamic polarization curves of 2205 DSS under 3.5 wt.% NaCl TEL

After tensile test, the specimen was descaled with nitric acid (100 mL of HNO_3 with distilled water added to 1000 mL), cleaned, and dried. Reduction-in-area and elongation were calculated according to the measurement of cross-sectional area and the length of the working segment before and after fracture. Finally, the fracture surfaces were observed using scanning electron microscope.

3. Results

3.1 Electrochemical Results

The potentiodynamic polarization curves of 2205 DSS with different HCCDs under 3.5 wt.% NaCl TEL are shown in Fig. 5. Hydrogen charging mainly promotes the anodic part of

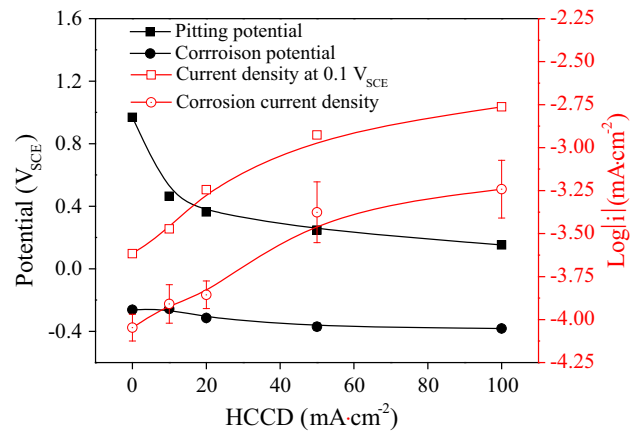


Fig. 6 Variation in electrochemical indexes obtained from the polarization curves (Fig. 5) with HCCD

polarization curves. With increased HCCD, the passivation current increases, and the pitting potential decreases, thereby decreasing the passive zone. Information obtained from Fig. 5, including pitting potential, corrosion potential, polarization current density at 0.1 V, and corrosion current density, was replotted against HCCD in Fig. 6. Corrosion potential and corrosion current density were obtained from the intersection of linear fitting lines of anodic and cathodic strong polarization zones in activation phase. With increased HCCD, the pitting potential and corrosion potential decrease at current density of 0.1 V, and the corrosion current density increases. Moreover, all the variation tendencies change slowly when HCCD exceeds 50 mA cm^{-2} . Hence, the uptake amount or the electrochemical effect of hydrogen may approach a limit when HCCD exceeds 50 mA cm^{-2} .

Figure 7 shows the EIS of 2205 DSS with different prior HCCDs under 3.5 wt.% NaCl TEL and the corresponding simulation circuit. The Nyquist curves exhibit a decreasing radius with increasing HCCD. This result indicates that the

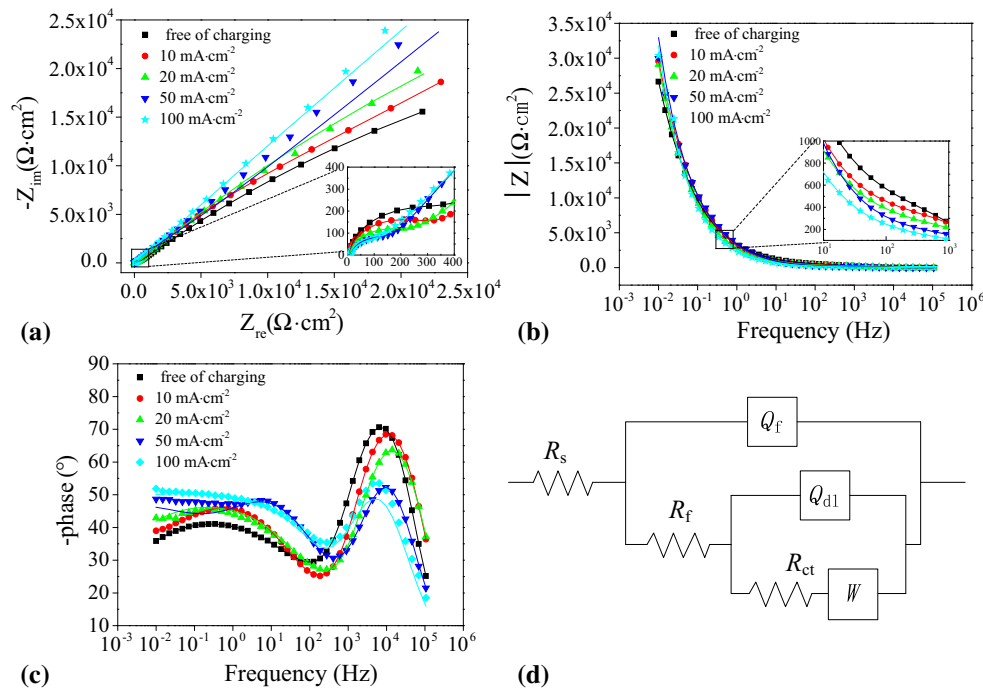


Fig. 7 Electrochemical impedance spectroscopy of 2205 DSS with different HCCDs under 3.5 wt.% NaCl TEL: (a) Nyquist curves, (b) bode absolute value against frequency, (c) bode phase value against frequency, and (d) the corresponding simulation circuit

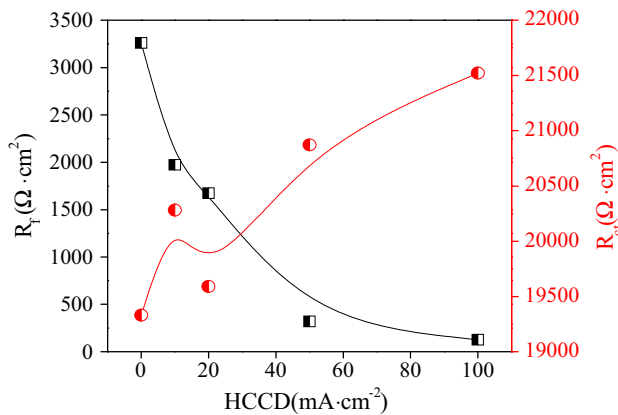


Fig. 8 Variation in passive film resistance and charge transfer resistance with HCCD

corrosion resistance of 2205 DSS decreases with increased HCCD. As shown in Fig. 7(b), R_s is the resistance of solution between reference electrode and working electrode, Q_f is the capacitance of passive film, R_f is the resistance of passive film, Q_{dl} is the capacitance of double layer, R_{ct} is the resistance of charge transfer, and W is the diffusion impedance. R_f and R_{ct} variations with HCCD are plotted in Fig. 8. R_f decreases remarkably with increased HCCD, whereas R_{ct} increases relatively slightly. Therefore, hydrogen charging suppresses the electrochemical reactivity, but weakens the passive film.

3.2 Hydrogen Determination

Hydrogen exists in metal matrix in the form of an atom. Driven by the anodic discharging electric field, the diffusible

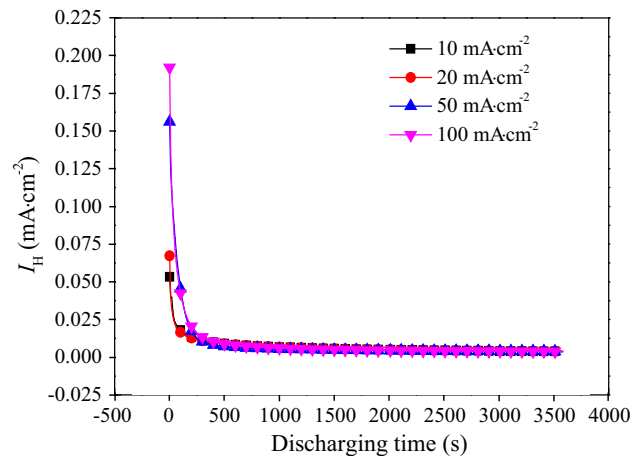


Fig. 9 Effect of HCCD on the hydrogen-oxidized current of 2205 DSS under 3.5 wt.% NaCl TEL

hydrogen in subsurface diffuses to the electric double layer; those hydrogen atoms, as well as some metal atoms, are oxidized to hydrogen anions. Consequently, the anodic oxidation current is generated. Hydrogen-oxidized current, I_H , can be obtained by subtracting the anodic oxidation current of the uncharged sample from that of the charged sample. Figure 9 shows the I_H variations at different prior HCCDs on discharging time. Evidently, I_H decreases markedly before 250 s and slowly after 250 s. This result indicates that hydrogen atoms are mainly absorbed on or near the metal surface. Thus, hydrogen charging may considerably influence the metal surface.

The damage caused by charging hydrogen can be quantified with the average concentration of the absorbed hydrogen in matrix (C_H). C_H is related to the corresponding quantity of electricity (Q):

Table 2 Hydrogen concentration absorbed in the substrate (C_H) under different HCCDs

HCCD, mA cm ⁻²	10	20	50	100
C_H (mol cm ⁻³)	8.110×10^{-7}	8.177×10^{-7}	9.837×10^{-7}	10.373×10^{-7}

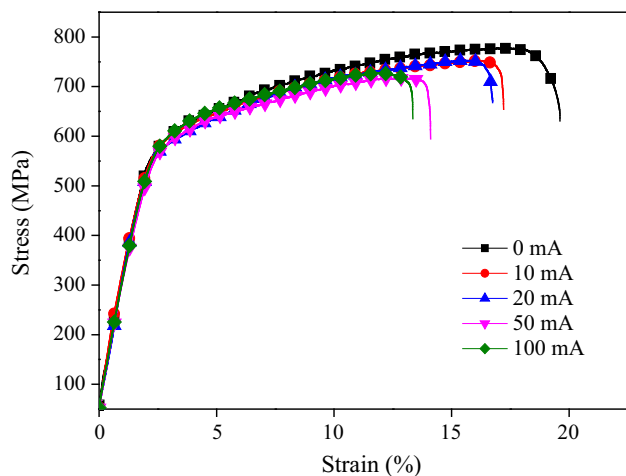


Fig. 10 Effect of HCCD on SSRT stress–strain curve of 2205 DSS under 3.5 wt.% NaCl TEL

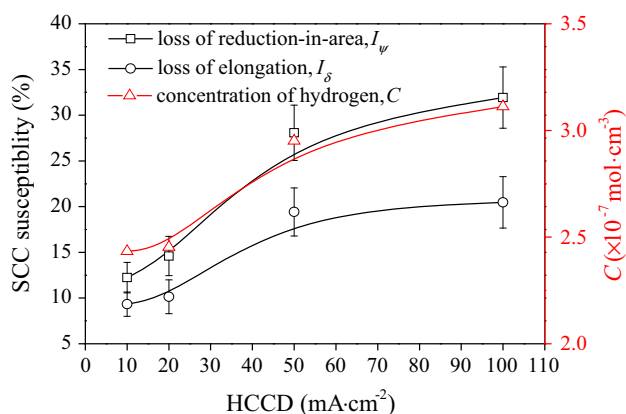


Fig. 11 Variation in stress corrosion cracking susceptibility and concentration of absorbed hydrogen in matrix (C_H) with HCCD

$$C_H = \frac{Q}{zFV}, \quad (\text{Eq 1})$$

where z is the electrons whose value for hydrogen atom is 1, F is the Faraday constant ($96487 \text{ C}\cdot\text{mol}^{-1}$), and V is the effective volume of the specimen (0.3 cm^3) in this study. Q in Coulomb is obtained by integrating I_H with respect to time, namely by calculating the area under the I_H curve (Ref 43).

$$Q = \int I_H dt. \quad (\text{Eq 2})$$

The C_H values under different HCCDs, integrated in the range of 0–3580 s, are listed in Table 2. Notably, C_H increases with increased HCCD. C_H values at different HCCDs are

replotted in Fig. 11. C_H immediately increases with increasing HCCD before 50 mA cm^{-2} and slowly from 50 to 100 mA cm^{-2} , which is consistent with the contents depicted in Fig. 6 and 8. Thus, the influence of HCCD on the electrochemical behavior of 2205 DSS under the TEL is directly related to the amount of hydrogen uptake. When HCCD exceeds 50 mA cm^{-2} , the amount of hydrogen uptake in 2205 DSS is close to saturation. Given the influence of hydrogen charging, this amount approaches a limit.

3.3 SSRT Tests After Various HCCDs

Figure 10 shows the stress–strain curves of 2205 DSS under different prior HCCDs at 3.5 wt.% NaCl TEL. The 2205 DSS elongation decreases with increased HCCD. The susceptibility of 2205 DSS to SCC is defined as the loss of reduction-in-area (I_ψ) or loss of elongation (I_δ):

$$I_\psi = (\psi_0 - \psi_m) / \psi_0 \times 100\% \quad (\text{Eq 3})$$

$$I_\delta = (\delta_0 - \delta_m) / \delta_0 \times 100\% \quad (\text{Eq 4})$$

where ψ_0 and ψ_m are reduction-in-area measured in air and under the TEL, and δ_0 and δ_m are elongation measured in air and under the TEL, respectively. Figure 11 depicts I_ψ , I_δ , and C_H together as a function of HCCD. The variation in I_ψ and I_δ with HCCD is consistent with that in C_H . Apparently, the SCC susceptibility of 2205 DSS directly correlates with hydrogen concentration in substrate.

Figure 12 shows the effect of prior HCCD on the fracture morphology of 2205 DSS in 3.5 wt.% NaCl TEL. The left and right sides are the macroscopic and microscopic views, respectively. Macroscopic images show that the necking degree of the fracture decreases with increasing HCCD. Microscopic images show an increasing brittle rupture with increasing HCCD. The fracture surface characteristic is a combination of dimples and cleavages. With increasing HCCD, the dimple area ratio increases. These results indicate that hydrogen charging remarkably increases the SCC susceptibility of 2205 DSS under the TEL.

The side surfaces of the SSRT specimens were also investigated and are shown in Fig. 12. Microcracks are observed on all side surfaces. Their numbers and lengths both increase with increased HCCD. Furthermore, few pits are observed on the side surface, and not all microcracks initiate from pits or any other form of localized corrosion. These results indicate that hydrogen charging promotes SCC susceptibility of 2205 DSS, mainly through HE rather than localized anodic dissolution. Moreover, the secondary cracks propagate straightly, not zigzag, which means that the crack propagation of 2205 DSS under 3.5 wt.% NaCl TEL is intergranular.

4. Discussion

4.1 Effect of Prior Hydrogen Charging on the Electrochemical Processes

The anodic reaction of 2205 DSS under 3.5 wt.% NaCl TEL is the following iron oxidation (Ref 11, 44):



The cathodic reaction is primarily the O_2 reduction:

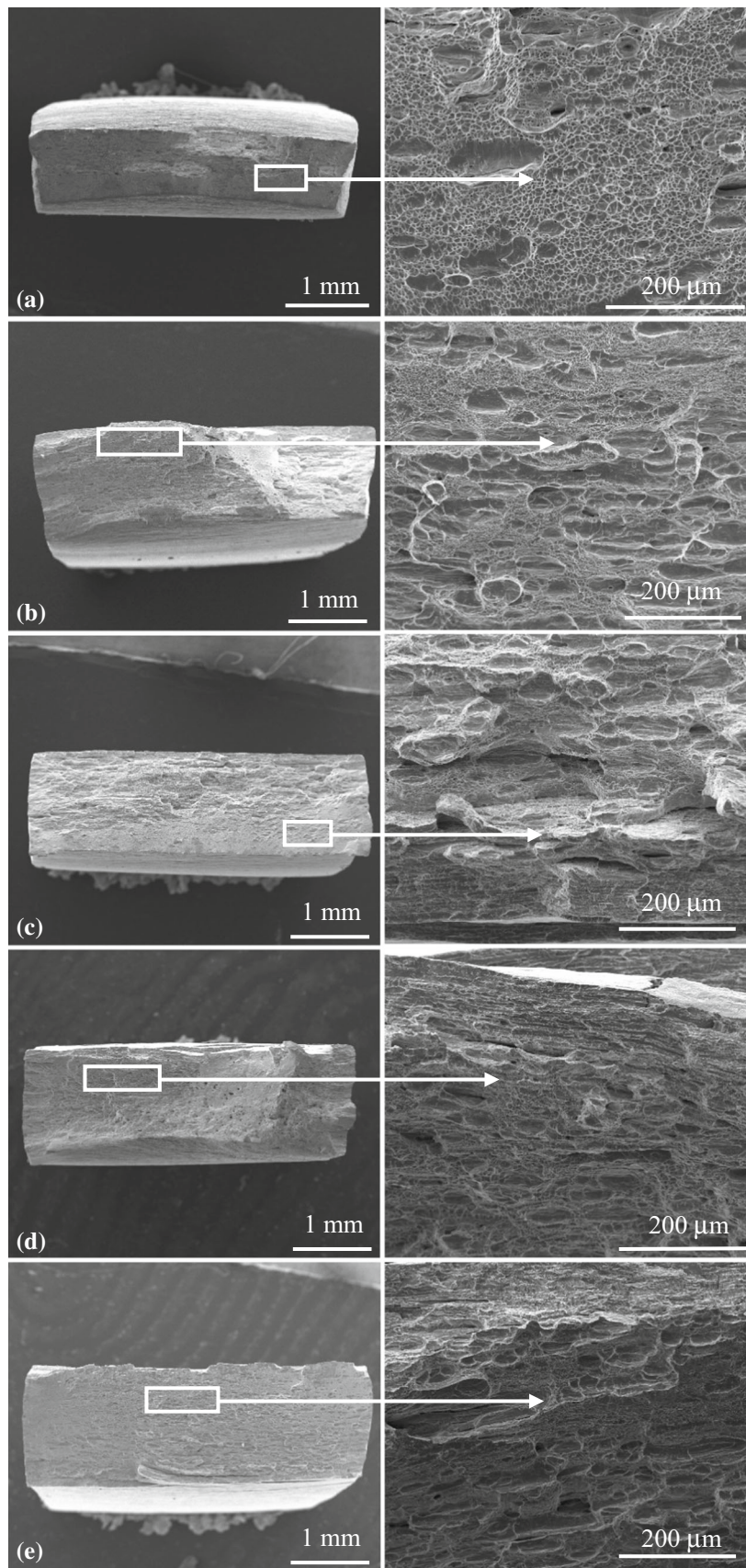


Fig. 12 Fracture morphologies of SSRT specimens under 3.5 wt.% NaCl TEL with different HCCDs: (a) 0, (b) 10, (c) 20, (d) 50, and (e) 100 mA cm⁻²

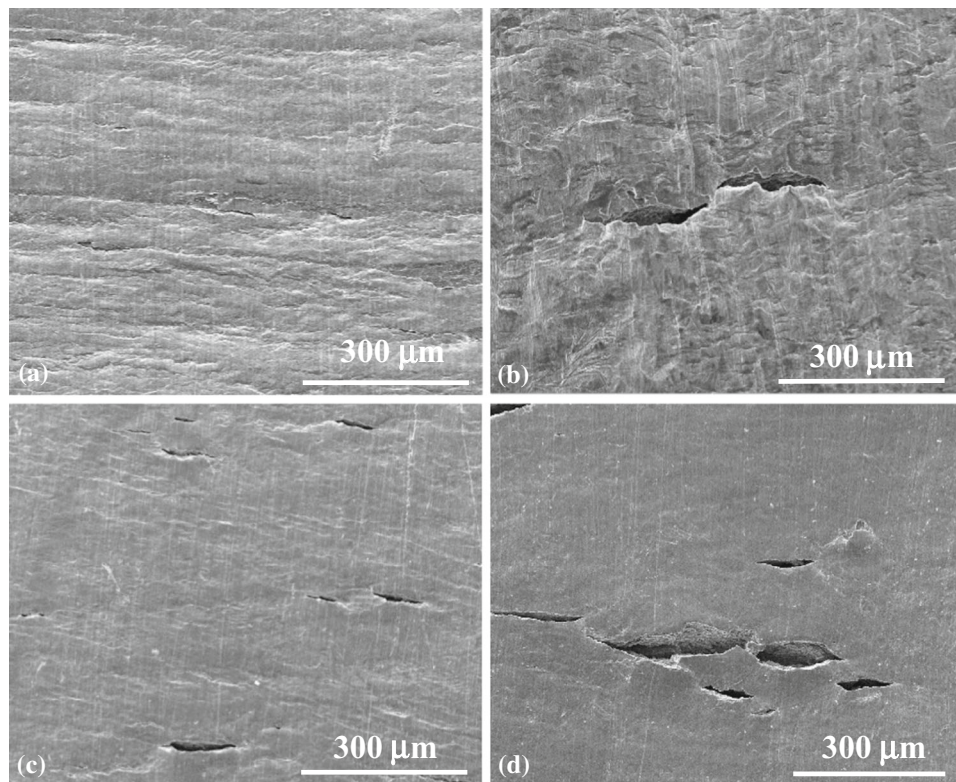
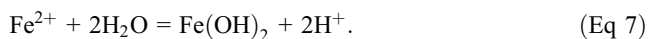


Fig. 13 Side morphologies of SSRT specimens under 3.5 wt.% NaCl TEL with different HCCDs: (a) 0, (b) 10, (c) 20, (d) 50, and (e) 100 mA cm⁻²



Furthermore, oxygen is exhausted in some localized areas, such as the interior of pit holes, crevices, and crack tips, where oxygen diffusion is impeded. These places are commonly called the blocking area. The anodic products (Fe^{2+} ions) inside these areas are hydrolyzed (Ref 11, 44):



In addition to the continual hydrolyzation of Fe^{2+} ions, the hydrogen ion in the blocking area is remarkably sufficient for hydrogen reduction:



In this reaction, hydrogen atoms are introduced electrochemically as a simulation of the produced hydrogen above. Figure 5 shows that hydrogen charging decreases the pitting resistance of 2205 DSS under the TEL. The uptake hydrogen increases the corrosion current density and passivation current density and decreases the passivation zone by decreasing the pitting potential. This phenomenon is also observed and explained by previous report about austenitic stainless steel (Ref 45). The charged hydrogen atoms hinder chromium enrichment in surface films. EIS results show that the effect of HCCD on electrochemical process is mainly weakening the R_f without increasing the R_{ct} (Fig. 7). This result indicates that the uptake hydrogen mainly blocks the formation of passive film rather than promotes the electrochemical reaction. This observation is verified on the side surfaces of SSRT specimens, where no obvious trace of anodic dissolution can be observed (Fig. 12). Generally, microcracks can be found inside the

corrosion pits when the SCC is induced by anodic dissolution; this observation is also demonstrated in many previous reports (Ref 46-48). Therefore, hydrogen charging influences the SCC behavior of 2205 DSS under the TEL by weakening the passive film without promoting localized anodic dissolution. Consequently, the weakened passive film allows the hydrogen atoms (produced in Eq 7) to permeate the matrix easily.

4.2 Effect of Prior Hydrogen Charging on the Stress Corrosion Behavior

Figures 10, 11, and 12 indicate that the SCC susceptibility of 2205 DSS increases with increased hydrogen concentration in the matrix. This result confirms that the SCC susceptibility of 2205 DSS under the TEL is closely related to hydrogen. Combined with the discussion in the last paragraph, hydrogen charging can be concluded to influence the SCC of 2205 DSS under TEL mainly through increasing its embrittlement. This result partly verifies that the SCC mechanism of 2205 DSS under the TEL is HE, when the conditions of localized hydrogen charging are available (Fig. 13).

Furthermore, it is noted that the susceptibility to HE of 2205 DSS under the TEL is highly consistent with hydrogen concentration in matrix. The SCC susceptibility increases more sharply when HCCD ranges from 20 to 50 mA cm⁻² than when HCCD is below 20 mA cm⁻² or above 50 mA cm⁻². It means that the uptake efficiency of hydrogen in matrix is enhanced when HCCD exceeds 20 mA cm⁻². There are two sources for this enhancement: ① One is that transformation of H_{ads} (Eq 8) to H_2 is depressed when HCCD exceeds 20 mA cm⁻² and ② the other one is that the passive film is weakened greatly so that hydrogen atoms can diffuse into the

matrix more easily. Generally, transformation of H_{ads} to H_2 will be not depressed, but promoted with increasing HCCD. So the first source cannot be the main reason. For the second source, Figure 8 shows that resistance of the passive film decreases greatly with increasing HCCD. It verifies the second source at a certain extent. Thus, it can be speculated that the weakened passive film results in the sharply enhancement of hydrogen uptake efficiency when HCCD ranges from 20 to 50 mA cm⁻².

It is also noted that the SCC susceptibility and hydrogen concentration increase slowly when the HCCD exceeds 50 mA cm⁻². This trend is assumingly attributed to the saturated hydrogen concentration in the substrate. Farrell (Ref 49) indicated that hydrogen concentration in ferrous alloys reaches a saturation level after prolonged charging. The saturation time and hydrogen concentration depend on charging conditions (electrolyte type, charging current, and charging temperature), type of steel, and sample geometry. However, other researchers believe that a considerably large number of hydrogen bubbles forming on the working electrode prevent the further introduction of hydrogen atoms (Ref 39). Thus, the reason of hydrogen saturation requires further investigation.

5. Conclusion

1. In this paper, the effects of hydrogen charging the stress corrosion behavior of 2205 duplex stainless steel have been investigated under 3.5 wt.% NaCl thin electrolyte layer. Based on the above results and discussions, the following conclusions can be drawn. 2205 DSS shows a nice resistance to pitting corrosion under hydrogen charging, although hydrogen weakens the passive film.
2. The stress corrosion mechanism of 2205 DSS under 3.5 wt.% NaCl TEL is mainly hydrogen embrittlement rather than localized anodic dissolution.
3. 2205 DSS shows a more susceptibility to hydrogen under the TEL when hydrogen charging current density is between 20 and 50 mA · cm⁻². Its SCC susceptibility increases remarkably when HCCD increases from 20 to 50 mA cm⁻² and slowly when HCCD exceeds 50 mA cm⁻².

Acknowledgments

This work was supported by the National High-Tech Research and Development Program of China (No. 2012AA040105), the National Nature Science Foundation of China (Nos. 51131001 and 51471034), and the Beijing Higher Education Young Elite Teacher Project.

References

1. X. Li, D. Zhang, Z. Liu, Z. Li, C. Du, and C. Dong, Materials Science: Share Corrosion Data, *Nature*, 2015, **527**, p 441–442
2. X. Liao, F. Cao, L. Zheng, W. Liu, A. Chen, J. Zhang, and C. Cao, Corrosion Behaviour of Copper under Chloride-containing Thin Electrolyte Layer, *Corros. Sci.*, 2011, **53**, p 3289–3298
3. Y.L. Cheng, Z. Zhang, F.H. Cao, J.F. Li, J.Q. Zhang, J.M. Wang, and C.N. Cao, A Study of the Corrosion of Aluminum Alloy 2024-T3 under Thin Electrolyte Layers, *Corros. Sci.*, 2004, **46**, p 1649–1667

4. G. Hinds and A. Turnbull, Threshold Temperature for Stress Corrosion Cracking of Duplex Stainless Steel under Evaporative Seawater Conditions, *Corrosion*, 2008, **64**, p 101–106
5. H.C. Ma, Z.Y. Liu, C.W. Du, H.R. Wang, X.G. Li, D.W. Zhang, and Z.Y. Cui, Stress Corrosion Cracking of E690 Steel as a Welded Joint in a Simulated Marine Atmosphere Containing Sulphur Dioxide, *Corros. Sci.*, 2015, **100**, p 627–641
6. T. Zhang, C. Chen, Y. Shao, G. Meng, F. Wang, X. Li, and C. Dong, Corrosion of Pure Magnesium under Thin Electrolyte Layers, *Electrochim. Acta*, 2008, **53**, p 7921–7931
7. H.R. Zhou, X.G. Li, J. Ma, C.F. Dong, and Y.Z. Huang, Dependence of the Corrosion Behavior of Aluminum Alloy 7075 on the Thin Electrolyte Layers, *Mater. Sci. Eng. B*, 2009, **162**, p 1–8
8. H.P. Wang, S.C. Ding, J. Zhu, Z. Zhang, J.Q. Zhang, and C.N. Cao, Corrosion Behavior of 907 Steel under Thin Electrolyte Layers of Artificial Seawater, *J. Cent. South Univ.*, 2015, **22**, p 806–814
9. Y. Huang and Y. Zhu, Hydrogen Ion Reduction in the Process of Iron Rusting, *Corros. Sci.*, 2005, **47**, p 1545–1554
10. Y. Huang, X. Dong, and J. Chen, Electrochemical Characteristics of an Austenitic Stainless Steel under Simulated Solution Film Formed in Marine Atmosphere, *Int. J. Electrochem. Sci.*, 2011, **6**, p 5597–5604
11. R. Nishimura, D. Shiraishi, and Y. Maeda, Hydrogen Permeation and Corrosion Behavior of High Strength Steel MCM 430 in Cyclic Wet-Dry SO₂ Environment, *Corros. Sci.*, 2004, **46**, p 225–243
12. E. Akiyama, S. Li, T. Shinohara, Z. Zhang, and K. Tsuzaki, Hydrogen Entry into Fe and High Strength Steels under Simulated Atmospheric Corrosion, *Electrochim. Acta*, 2011, **56**, p 1799–1805
13. E. Akiyama, K. Matsukado, M. Wang, and K. Tsuzaki, Evaluation of Hydrogen Entry into High Strength Steel under Atmospheric Corrosion, *Corros. Sci.*, 2010, **52**, p 2758–2765
14. R.B. Hamzah and M.J. Robinson, Hydrogen Absorption Resulting from the Simulated Pitting Corrosion of Carbon-Manganese Steels, *Corros. Sci.*, 1987, **27**, p 971–979
15. J.R. Galvele, Tafel's Law in Pitting Corrosion and Crevice Corrosion Susceptibility, *Corros. Sci.*, 2005, **47**, p 3053–3067
16. A.D. Keitelman, S.M. Gravano, and J.R. Galvele, Localized Acidification as the Cause of Passivity Breakdown of High Purity Zinc, *Corros. Sci.*, 1984, **24**, p 535–545
17. H. Ma, C. Du, Z. Liu, W. Hao, X. Li, and C. Liu, Stress Corrosion Behaviors of E690 High-strength Steel in SO₂-polluted Marine Atmosphere, *Acta Metall. Sin.*, 2016, **52**, p 331–340
18. S. Li, Z. Zhang, E. Akiyama, K. Tsuzaki, and B. Zhang, Evaluation of Susceptibility of High Strength Steels to Delayed Fracture by Using Cyclic Corrosion Test and Slow Strain Rate Test, *Corros. Sci.*, 2010, **52**, p 1660–1667
19. T. Tsuru, Y. Huang, M.R. Ali, and A. Nishikata, Hydrogen Entry Into Steel During Atmospheric Corrosion Process, *Corros. Sci.*, 2005, **47**, p 2431–2440
20. D. Zhang and Y. Li, Effect of Humidity on Hydrogen Embrittlement Susceptivity of Hot-dip Galvanized Steel Exposed to Simulated Marine Atmosphere, *China Nonferrous Met.*, 2010, **20**, p 476–482
21. H. Luo, C.F. Dong, K. Xiao, and X.G. Li, Characterization of Passive Film on 2205 Duplex Stainless Steel in Sodium Thiosulphate Solution, *Appl. Surf. Sci.*, 2011, **258**, p 631–639
22. J. Lv, T. Liang, C. Wang, and L. Dong, Effect of Ultrafine Grain on Tensile Behaviour and Corrosion Resistance of the Duplex Stainless Steel, *Mater. Sci. Eng. C*, 2016, **62**, p 558–563
23. C. Örnek and D.L. Engelberg, Towards Understanding the Effect of Deformation Mode on Stress Corrosion Cracking Susceptibility of Grade 2205 Duplex Stainless Steel, *Mater. Sci. Eng. A*, 2016, **666**, p 269–279
24. L.Q. Guo, Y. Bai, B.Z. Xu, W. Pan, J.X. Li, and L.J. Qiao, Effect of Hydrogen on Pitting Susceptibility of 2507 Duplex Stainless Steel, *Corros. Sci.*, 2013, **70**, p 140–144
25. W.T. Tsai and M.S. Chen, Stress Corrosion Cracking Behavior of 2205 Duplex Stainless Steel in Concentrated NaCl Solution, *Corros. Sci.*, 2000, **42**, p 545–559
26. W.T. Tsai and S.L. Chou, Environmentally Assisted Cracking Behavior of Duplex Stainless Steel in Concentrated Sodium Chloride Solution, *Corros. Sci.*, 2000, **42**, p 1741–1762
27. A.A. El-Yazgi and D. Hardie, The Embrittlement of a Duplex Stainless Steel by Hydrogen in a Variety of Environments, *Corros. Sci.*, 1996, **38**, p 735–744

28. A. Turnbull, P. Nicholson, and S. Zhou, Chemistry of Concentrated Salts Formed by Evaporation of Formation Water and the Impact on Stress Corrosion Cracking of Duplex Stainless Steel, *Corrosion*, 2007, **63**, p 555–560
29. C. Örnek, S.A.M. Idris, P. Reccagni, and D.L. Engelberg, Atmospheric-Induced Stress Corrosion Cracking of Grade 2205 Duplex Stainless Steel-Effects of 475°C Embrittlement and Process Orientation, *Metals*, 2016, **6**, p 167–188
30. L. Wang, Y. Xing, Z. Liu, D. Zhang, C. Du, and X. Li, Erosion-Corrosion Behavior of 2205 Duplex Stainless Steel in Wet Gas Environments, *J. Nat. Gas Sci. Eng.*, 2016, **35**, p 928–93427
31. A. Glowacka and W.A. Świtnicki, Effect of Hydrogen Charging on the Microstructure of Duplex Stainless Steel, *J. Alloys Compd.*, 2003, **356–357**, p 701–704
32. T. Zakroczyński, A. Glowacka, and W. Światnicki, Effect of Hydrogen Concentration on the Embrittlement of a Duplex Stainless Steel, *Corros. Sci.*, 2005, **47**, p 1403–1414
33. T. Zakroczyński and E. Owczarek, Electrochemical Investigation of Hydrogen Absorption in a Duplex Stainless Steel, *Acta Mater.*, 2002, **50**, p 2701–2713
34. E. Owczarek and T. Zakroczyński, Hydrogen Transport in a Duplex Stainless Steel, *Acta Mater.*, 2000, **48**, p 3059–3070
35. W.C. Luu, P.W. Liu, and J.K. Wu, Hydrogen Transport and Degradation of a Commercial Duplex Stainless Steel, *Corros. Sci.*, 2002, **44**, p 1783–1791
36. N. Kheradmand, R. Johnsen, J.S. Olsen, and A. Barnoush, Effect of Hydrogen on the Hardness of Different Phases in Super Duplex Stainless Steel, *Int. J. Hydrogen Energy*, 2015, **41**, p 1106–1107
37. R. Silverstein, O. Sobol, T. Boellinghaus, W. Unger, and D. Eliezer, Hydrogen Behavior in SAF 2205 Duplex Stainless Steel, *J. Alloys Compd.*, 2016, **695**, p 2689–2695
38. R. Silverstein, D. Eliezer, B. Glam, S. Eliezer, and D. Moreno, Evaluation of Hydrogen Trapping Mechanisms During Performance of Different Hydrogen Fugacity in a Lean Duplex Stainless Steel, *J. Alloys Compd.*, 2015, **648**, p 601–608
39. C.F. Dong, Z.Y. Liu, X.G. Li, and Y.F. Cheng, Effects of Hydrogen-Charging on the Susceptibility of X100 Pipeline Steel to Hydrogen-Induced Cracking, *Int. J. Hydrog. Energy*, 2009, **34**, p 9879–9884
40. Z.Y. Liu, C.F. Dong, X.G. Li, Q. Zhi, and Y.F. Cheng, Stress Corrosion Cracking of 2205 Duplex Stainless Steel in H₂S–CO₂ Environment, *J. Mater. Sci.*, 2009, **44**, p 4228–4234
41. B.T. Lu, L.J. Qiao, J.L. Luo, and K.W. Gao, Role of Hydrogen in Stress Corrosion Cracking of Austenitic Stainless Steels, *Philos. Mag.*, 2011, **91**, p 208–228
42. Y. Yao, L.J. Qiao, and A.A. Volinsky, Hydrogen Effects on Stainless Steel Passive Film Fracture Studied by Nanoindentation, *Corros. Sci.*, 2011, **53**, p 2679–2683
43. M. Yan and Y. Weng, Study on Hydrogen Absorption of Pipeline Steel under Cathodic Charging, *Corros. Sci.*, 2006, **48**, p 432–444
44. C.W. Du, T.L. Zhao, Z.Y. Liu, X.G. Li, and D.W. Zhang, Corrosion Behavior and Characteristics of the Product Film of API, X100 Steel in Acidic Simulated Soil Solution, *Int. J. Miner. Metall. Mater.*, 2016, **23**, p 176–183
45. L.J. Qiao and J.L. Luo, Hydrogen-facilitated Anodic Dissolution of Austenitic Stainless Steels, *Corrosion*, 1998, **54**, p 281–288
46. F. Delaunois, A. Tshimombo, V. Stanciu, and V. Vitry, Monitoring of Chloride Stress Corrosion Cracking of Austenitic Stainless Steel: Identification of the Phases of the Corrosion Process and Use of a Modified Accelerated Test, *Corros. Sci.*, 2016, **110**, p 273–283
47. B.T. Lu, Z.K. Chen, J.L. Luo, B.M. Patchett, and Z.H. Xu, Pitting and Stress Corrosion Cracking Behavior in Welded Austenitic Stainless Steel, *Electrochim. Acta*, 2005, **50**, p 1391–1403
48. X.W. Lei, Y.R. Feng, A.Q. Fu, J.X. Zhang, Z.Q. Bai, C.X. Yin, and C.H. Lu, Investigation of Stress Corrosion Cracking Behavior of Super 13Cr Tubing by Full-Scale Tubular Goods Corrosion Test System, *Eng. Fail. Anal.*, 2015, **50**, p 62–70
49. K. Farrell, Cathodic Hydrogen Absorption and Severe Embrittlement in a High Strength Steel, *Corrosion*, 1970, **26**, p 105–110